Available online at www.sciencedirect.com
ScienceDirect
Earth and Planetary Science Letters 252 (2006) 423–436
EPSL
www.elsevier.com/locate/epsl

Origin of high-Al N-MORB by fractional crystallization in the upper mantle beneath the Galápagos Spreading Center

Deborah Eason *, John Sinton

Department of Geology and Geophysics, School of Ocean and Earth Science and Technology, University of Hawaii, Honolulu, HI, USA

Received 24 May 2006; received in revised form 30 September 2006; accepted 30 September 2006
Available online 15 November 2006
Editor: R.W. Carlson

Abstract

The Galápagos Spreading Center (GSC) includes lavas with chemical compositions ranging from N-MORB to transitional and more enriched MORB. N-MORB dominate the region west of 95.5°W, far from the influence of the Galápagos hotspot. However, some N-MORB glass samples from the GSC have very high Al contents (>16.0 wt.% Al_2O_3 at >8.5 wt.% MgO), similar to high-Al N-MORB from other slow and intermediate spreading ridges and close to fracture zones elsewhere. GSC high-Al N-MORB are dominated mineralogically by uniform plagioclase compositions (An 80–82) with only 1–2% olivine (Fo 85–87), and have glass compositions with higher Al_2O_3 and lower SiO_2 than is predicted by normal MORB fractionation trends. Forward modeling using the MELTS and pMELTS algorithms constrained by crustal thickness measurements indicates that high-Al, low-Si MORB can be produced by high-pressure crystallization in the upper mantle using the same source as normal (low-Al) GSC N-MORB. Although high-Al glasses can be obtained by very low extents of partial melting of this mantle source, such melting models result in significant misfits in other major element oxides, especially SiO_2. Models involving significant evolution with up to 20% olivine and clinopyroxene crystallization at pressures of 0.3–0.4 GPa can account for the complete major and selected trace element compositions of these unusual MORB samples. We suggest that high-pressure fractionation is enhanced by conductive cooling of the upper mantle in this area of the GSC, consistent with other recent models correlating mantle crystallization with slow spreading mid-ocean ridges and fracture zones.

Keywords: MORB; mid-ocean ridge; Galápagos rift; basalt fractionation; pMELTS; mantle

1. Introduction

The nearly east–west trending GSC separates the Cocos and Nazca plates in the eastern equatorial Pacific (Fig. 1). Samples from this study were collected during the Galápagos Plume Ridge Interaction Multidisciplinary Experiment (G-PRIME), which included detailed bathymetric mapping, and the collection of seismic refraction, reflection, and magnetics data and rock samples along an ~800 km-long portion of the ridge extending from 90.5°W, just north of the Galápagos Archipelago and the inferred location of the Galápagos mantle plume, to 98°W, the region of the GSC considered to be a "normal" mid-ocean ridge [1]. Full spreading rates along this portion of the ridge vary from 46 mm/yr at 98°W to 56 mm/yr at 91°W near the Galápagos hotspot [2].

* Corresponding author. Tel.: +1 808 956 9544.
E-mail address: deborahe@hawaii.edu (D. Eason).

0012-821X/$ - see front matter © 2006 Elsevier B.V. All rights reserved.
doi:10.1016/j.epsl.2006.09.048

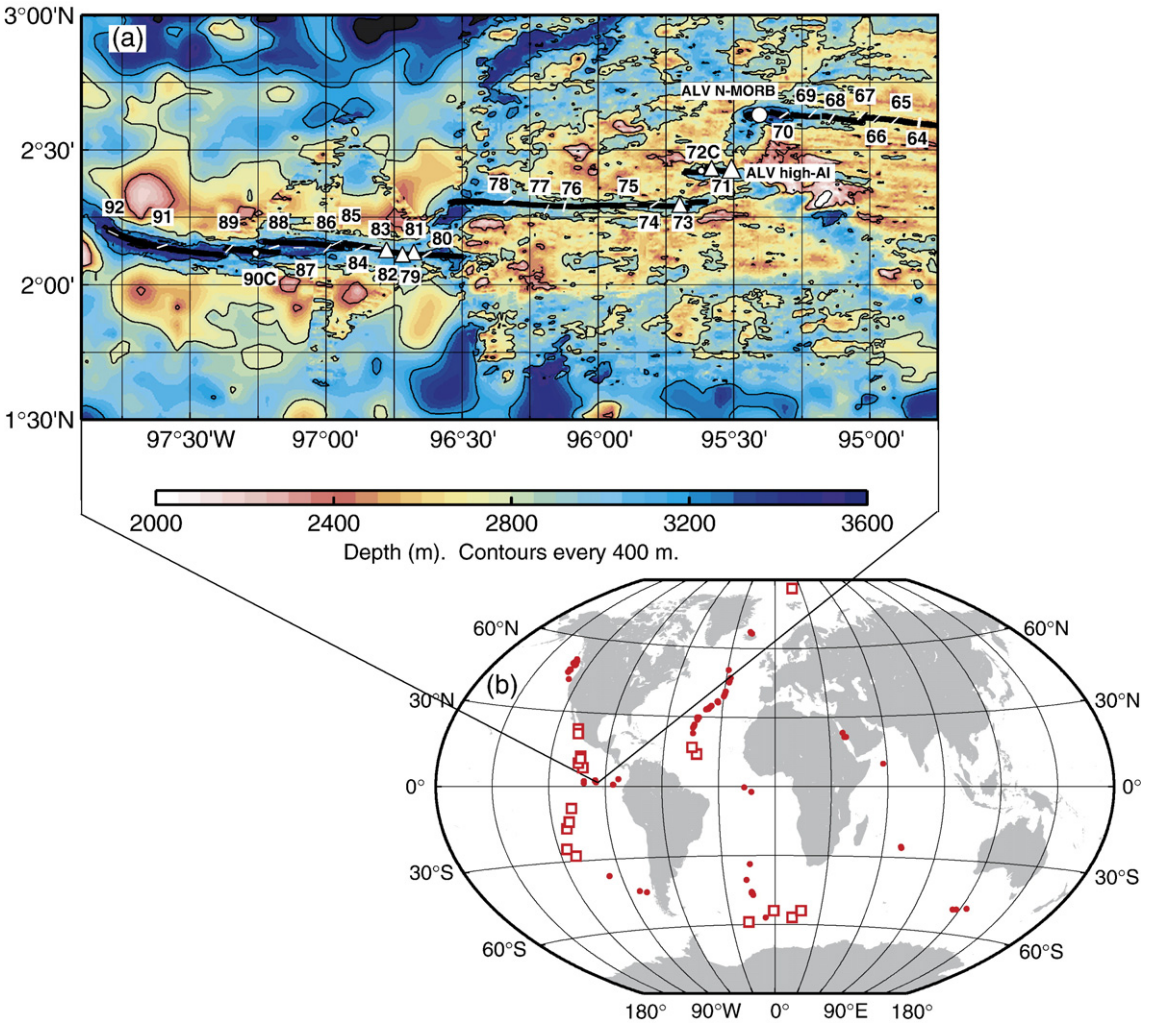

Fig. 1. (a) Sample locations along part of the western Galápagos Spreading Center. Station numbers are those for the G-PRIME expedition [1,3]. ALVIN (ALV) samples from Hey et al. [63]. High-Al sample locations are shown as triangles. Thick black line denotes the GSC axis from Sinton et al. [63]. (b) Global distribution of samples in PetDB [64] with $Al_2O_3 > 16.0$ wt.%, MgO > 8.5 wt.%. Open squares denote fracture zone samples.

The G-PRIME sample suite includes chemical compositions varying from normal (N-) to transitional (T-) and more enriched (E-) mid-ocean ridge basalts (MORB) [1,3]. N-MORB dominate the area west of the propagating rift at 95.5°W, which appears to be the limit of geochemical influence of the Galápagos hotspot. Samples west of the propagating rift show little or no evidence of plume enrichment, while samples to the east show increasing incompatible element and isotopic enrichment approaching the plume (~91.7°W) [3–7].

Galápagos N-MORB are characterized by moderate to high MgO values (ranging from 6.9 wt.% MgO to nearly 10 wt.% MgO) and low concentrations of elements that are incompatible during mantle melting (≤0.08 wt.% K_2O, 1.67–2.56 wt.% Na_2O, 0.77–1.68 wt.% TiO_2, 0.05–0.12 wt.% P_2O_5), with K/Ti ratios <0.09. GSC N-MORB also have low water contents (no greater than 0.22 wt.% H_2O, with an average of 0.16 wt.% H_2O). Cushman et al. [3] argued that average Galápagos N-MORB could be produced from a mean fraction of partial melting ($\bar{F}$) ~0.06 of a source with ~34±1 ppm K, 133±3 ppm H_2O, 2250±50 ppm Na_2O, and 1050±25 ppm Ti.

Some of the N-MORB glass samples from the GSC have unusually high Al_2O_3 contents (>16.0 wt.%) at MgO > 8.5 wt.%. These samples have higher aluminum and lower silica than predicted by normal MORB fractionation trends while maintaining very low potassium and sodium values. According to MELTS models of their glass compositions [8], they are saturated with

plagioclase at low pressures even at MgO>9.0 wt.%, consistent with experimental data reported for other high-Al MORB (e.g., [9,10]). High-MgO basalts with unusually high aluminum content also have been reported for various mid-ocean ridges (see Fig. 1), although their origin is not fully understood (e.g., [11–13]). These high-Al MORB are distinct from the high-Al basalts and andesites often associated with arcs, which tend to be more evolved with higher K and H_2O contents. Such high-Al, low-Si basalts appear to be restricted to ridges with slow spreading rates or close to fracture zones and ridge terminations. Along the GSC, high-Al samples are located close to ridge segment ends or associated with failing rifts (Fig. 1).

The extensive dataset available from G-PRIME makes the Galápagos an ideal location to examine the melting and fractionation processes that give rise to high-Al MORB compositions. Glass data for the sample suite were reported in Cushman et al. [3], and whole-rock XRF data are reported for Galápagos N-MORB in Table 1. Estimates of GSC crustal thickness from multichannel seismic reflection data [1,14] put a limit on melt productivity, giving us an important modeling constraint.

To supplement the glass and whole rock analyses, we collected mineral compositions, zoning profiles, and modes in five high-Al GSC samples. Using this combination of petrographic and chemical data, we are able to model the feasibility of various melting and fractionation paths using the MELTS and pMELTS algorithms [8,15–17] by comparing the phase compositions and abundances resulting from each evolution path with the chemistry of the rocks themselves. We first establish a working model that produces the array of normal GSC N-MORB under reasonable ridge melting and crystallization conditions, then use the determined source composition to model the evolution of the high-Al samples. By varying the pressure and extent of partial melting of the GSC source as well as the pressure and extent of subsequent fractional crystallization of these hypothetical parental magmas, we can constrain 1) possible source depths that the high-Al magmas could be generated, 2) the range of partial melting that allow these high-Al compositions, and 3) the range of depths where these magmas may have evolved. This forward modeling approach allows us to eliminate impossible processes and constrain ridge melting and evolution to a restricted range of conditions.

2. Data and methods

Whole rock x-ray fluorescence (XRF) data were measured on the University of Hawaii Siemens 303 AS XRF spectrometer using a Rh-target, end-window x-ray tube. Whole rocks were crushed in an alumina swing mill, and powders were analyzed for major elements on fused disks following methods similar to those of Norrish and Hutton [18]. Trace elements were analyzed on pressed powder pellets. Peak intensities for the trace elements were corrected for backgrounds, line interferences and matrix absorption using methods similar to Chappell [19]. Corrected intensities were calibrated against a wide range of natural rock standards. Accuracy and precision data for this system are reported in Sinton et al. [20].

Glass and mineral compositions were collected using the University of Hawaii Cameca SX-50 five-spectrometer electron microprobe. Major and minor element analyses for GSC glasses are reported in Cushman et al. [3]. Mineral analyses reported here are averages of three spots collected from individual crystals in selected high-Al MORB. Plagioclase was analyzed for Si, Al, Fe, Mg, Ca, Na and K using an accelerating voltage of 15 kV, 20 nA beam current, and 10 μm beam diameter. Peak counting times were 30 s for Si, Mg, Al, and Na and 60 s for Fe, Ca, and K. Background counting times were 30 s for Fe, Ca, and K; 15 s for Si, Mg, and Al; and 20 s for Na. Na was analyzed first in each acquisition to minimize loss due to volatilization. Samples were calibrated against mineral standards Lake County plagioclase (Si and Al), San Carlos olivine (Fe and Mg), Amelia albite (Na), anorthite (Ca) and orthoclase (K). A PAP–ZAF matrix correction was applied to all analyses.

Olivine was analyzed for Si, Mg, Fe, Ca, Mn and Ni using an accelerating voltage of 20 kV, 30 nA beam current, and 10 μm beam diameter. Peak counting times were 60 s for Mg and Si; 80 s for Ca and Ni; 50 s for Fe; and 40 s for Mn. Background counting times were 30 s for Mg and Si; 40 s for Ca and Ni; 25 s for Fe; and 20 s for Mn. Samples were calibrated against San Carlos olivine (Mg), Springwater olivine (Fe), Verma garnet (Mn), diopside (Si and Ca) and Ni–metal (Ni) standards. A PAP–ZAF matrix correction was applied to all analyses.

It should be noted that the whole-rock Na content is consistently lower than the glass Na for the same rock, possibly indicating partial volatilization of Na during fusion as part of the XRF sample preparation for major elements. This does not affect the results presented in subsequent sections, as all modeling is done using glass Na content rather than whole-rock data.

Thin sections were examined for textural indications of disequilibrium and 1000-point counts were collected on selected high-Al samples to determine mineral modes (see Supplementary material). Mineral grains <0.05 mm in size appear to have crystallized post-eruption, and are considered “groundmass” for counting purposes, so that

Table 1
Whole-rock XRF analyses for GSC N-MORB, incl. G-PRIME (EW), Alvin (AL) and Atlantis (A) samples [62]

Sample	SiO_2	TiO_2	Al_2O_3	$Fe_2O_3^*$	MnO	MgO	CaO	Na_2O	K_2O	P_2O_5	Sum	Sc	V	Cr	Co	Ni	Cu	Zn	Rb	Sr	Y	Zr	Nb	Long	Lat	Depth
EW43-1	49.72	0.92	14.82	10.37	0.16	8.66	13.28	1.52	0.04	0.07	99.56	48	307	338	48	98		72	1.5	63	21	43	2.0	−93.257	2.414	2243
EW63-1	49.68	1.16	15.41	11.11	0.17	8.12	12.48	1.80	0.05	0.08	100.04	44	336	343	45	113		83	1.8	71	28	63	2.4	−94.747	2.594	2655
EW63-2	48.88	1.27	15.64	12.12	0.18	8.05	11.84	2.09	0.09	0.09	100.24	45	286	295	48	115		88	2.3	100	28	73	3.8	−94.747	2.594	2655
EW71-1	48.64	1.01	15.80	10.34	0.17	9.77	12.17	2.13	0.06	0.07	100.15	46	271	520	52	211		66	1.4	95	24	59	1.8	−95.602	2.425	2768
EW71-4	48.76	1.01	15.70	10.52	0.17	9.87	12.24	1.75	0.04	0.07	100.13	46	266	533	52	228		67	1.5	95	25	59	1.9	−95.602	2.425	2768
EW77-2	49.63	1.17	15.60	10.61	0.17	8.17	12.67	1.92	0.04	0.08	100.05	46	323	387	45	111		78	1.2	85	27	65	1.9	−96.191	2.281	2851
EW79-1	48.22	0.97	17.29	10.41	0.15	8.98	11.94	2.23	0.04	0.07	100.30	35	216	326	48	169		73	1.1	110	21	53	1.9	−96.725	2.100	3136
EW80-2	49.41	1.10	16.04	10.06	0.16	8.76	12.67	2.08	0.02	0.06	100.35	43	263	443	46	137		71	0.9	91	26	62	1.1	−96.630	2.115	3071
EW81-3	48.38	0.89	17.10	9.20	0.15	9.69	12.48	2.04	0.02	0.05	99.98	39	221	468	50	203		62	1.2	92	22	50	1.7	−96.697	2.120	3062
EW82-8	47.77	1.00	17.70	9.99	0.15	9.28	12.17	2.09	0.02	0.05	100.22	42	195	325	49	201		63	0.6	113	23	61	0.9	−96.775	2.122	3025
EW83-5	49.50	1.25	15.73	10.74	0.17	8.71	12.14	1.91	0.04	0.08	100.25	44	300	405	47	154		80	1.4	84	30	70	1.9	−96.818	2.138	2957
EW84-2	49.86	1.21	15.05	10.91	0.17	8.42	12.12	1.72	0.04	0.09	99.59	44	308	388	48	124		82	1.4	83	31	74	3.0	−96.877	2.139	3042
EW87-1	49.89	1.11	15.79	10.12	0.16	8.62	12.66	1.87	0.03	0.07	100.31	44	280	458	44	140		73	1.1	80	27	62	1.6	−97.100	2.139	3272
EW88-1	50.02	1.15	15.42	10.42	0.16	8.38	12.55	2.10	0.05	0.09	100.33	41	292	464	45	129		74	1.2	76	28	64	2.0	−97.192	2.142	3229
EW91-6	49.71	1.05	15.42	10.37	0.16	9.05	12.35	1.81	0.04	0.06	100.02	43	285	453	47	160		75	1.5	75	26	60	1.7	−97.604	2.145	3440
EW92-1	49.77	1.40	15.13	11.04	0.17	8.42	11.69	1.95	0.07	0.12	99.74	44	338	355	47	135		83	1.3	87	33	87	2.4	−97.782	2.193	3360
AL-1545-4	49.66	0.99	15.87	10.70	0.16	9.00	12.54	1.50	0.04	0.10	100.56	42	286	496	47	161	83	76	1.3	70	25	55	2.0	−95.37	2.63	3229
AL-1545-6	49.60	0.99	15.92	10.81	0.16	8.98	12.58	1.51	0.04	0.11	100.70	44	289	501	48	163	85	76	1.2	70	24	55	1.9	−95.38	2.63	3145
AL-1549-3	49.63	0.98	15.86	10.66	0.16	9.08	12.57	1.55	0.04	0.10	100.63	42	288	497	46	167	85	77	1.1	70	24	55	2.1	−95.38	2.63	3176
AL-1549-4	49.73	0.95	15.10	10.57	0.16	8.92	12.59	1.81	0.05	0.05	99.93	44	284	502	46	175	89	80	1.6	76	26	59	2.1	−95.38	2.63	3172
AL-1549-5	49.48	0.92	14.93	10.51	0.16	9.07	12.51	1.80	0.04	0.05	99.47	43	291	493	44	165	85	77	1.0	70	24	55	2.1	−95.38	2.63	3181
AL-1550-2	49.98	0.84	15.77	9.37	0.15	9.11	12.89	1.95	0.05	0.04	100.15	40	239	621	42	163	79	64	1.0	83	21	47	2.0	−95.54	2.36	2270
AL-1551-3	49.02	1.07	15.97	9.81	0.15	9.10	12.21	2.44	0.06	0.05	99.88	41	248	490	46	175	81	67	0.9	118	24	68	1.7	−95.48	2.41	3063
AL-1552-8	48.77	1.00	15.61	10.82	0.16	9.45	11.96	1.97	0.03	0.05	99.82	42	264	398	48	197	79	74	1.2	75	27	57	1.8	−95.53	2.38	2274
AL-1554-1	48.56	1.03	15.50	10.28	0.15	9.99	11.72	2.16	0.04	0.05	99.48	40	256	519	47	227	81	70	1.1	91	25	64	2.2	−95.48	2.42	2912
A3-A	50.19	1.06	15.45	10.26	0.16	8.61	12.35	1.77	0.06	0.09	99.99	44	297	445	46	140		73	1.8	85	25	59	2.4	−95.53	2.37	2575
A3-B	49.48	0.95	16.42	9.28	0.14	8.79	12.61	1.73	0.04	0.07	99.51	42	239	530	43	161		66	1.3	87	22	51	1.9	−95.53	2.37	2575
A13-2	49.95	1.15	15.64	10.45	0.16	8.01	12.31	1.75	0.06	0.09	99.55	43	314	388	44	122		76	1.8	81	26	62	2.6	−95.62	2.31	3060

Oxide abundances given in wt.%, trace elements in ppm. Depth given as mbsl.
*Total Fe as Fe_2O_3.
Negative loss on ignition at 900 °C for all samples. Ba, Pb, Th, U are below detection limits, averaging 10, 2, 1.3, and 1.5 ppm respectively.

our mode reflects the phenocryst assemblage rather than evolution after eruption.

Forward modeling of the samples' geochemical evolution was done primarily using Adiabat_1ph [17], the latest release of the MELTS and pMELTS algorithms for thermodynamic modeling of phase equilibria in magmatic systems [8,16]. Also included in this release is pHMELTS, which models the effects of water storage in nominally anhydrous minerals using trace element partitioning to distribute H_2O between the system and a separate hidden reservoir [21].

3. Mineralogy

The high-Al MORB samples range from nearly aphyric to ~18% phenocrysts (see Supplementary material). Phenocryst assemblages are dominated by sub- to euhedral plagioclase, comprising up to 90% of the mineral mode, or up to 15% of the total rock mode. Plagioclase phenocrysts are tabular to elongate, up to 2 mm in width. These rocks also contain a small amount of olivine (1–2%) as sub- to euhedral grains, <1 mm across. Mineral compositions are fairly uniform across the sample suite, with plagioclase compositions averaging ~An 80–82 and olivine compositions of Fo 85–87. Profiles across plagioclase grains indicate a small degree of zoning, which can be both normal and reverse within a given sample. There is no textural evidence of disequilibrium, such as strong zoning or resorption, that might indicate a process such as plagioclase assimilation. Some plagioclase grains contain melt inclusions, but they are too devitrified to yield good glass compositions. While most plagioclase phenocrysts are euhedral, a few are fractured and less well-formed, although there does not appear to be a compositional distinction between the two types. The groundmass in these samples ranges from glassy to cryptocrystalline with abundant microspherulites. EW 82-8 contains small clinopyroxene grains up to 0.05 mm across associated with radial plagioclase glomerocrysts in the groundmass, but there are no phenocrysts of clinopyroxene in any of the high-Al samples.

4. Galápagos N-MORB

We use a two-stage forward model to determine a reasonable GSC mantle source composition appropriate to our rock chemistry. In the first stage, we model melting processes using pHMELTS, constrained by a target crustal thickness of $Z_c \sim 5.6$–6.0 km [1,14]. Melting runs simulate adiabatic decompression, setting entropy, S, (or potential temperature, T_0) to control the depth at which the solidus is reached and melting begins. Melting is treated as continuous, where a small fraction (0.005) of melt is retained at each extraction step. Model melting continues to the base of the crust, where the fractional melts are then aggregated. We assume passive mantle upwelling, integrating for a 2-D (triangular) melting regime to form our aggregate melts [22]. In stage two of the model, these aggregate melts are cooled at 1.0 kb, appropriate to crustal depths. We model crystallization using the MELTS calibration, which is more accurate at low pressure. Crystallization runs are isobaric and fractional, with an oxygen fugacity setting of FMQ-2. Major element compositional modeling includes SiO_2, TiO_2, Al_2O_3, FeO*, MgO, CaO, and Na_2O. K_2O and P_2O_5 content have an unrealistically strong effect on the solidus depth when treated as major elements in pMELTS calculations, so we model them here as trace elements. We have also included additional trace elements (Cr, V, Sc and Sr) using partition coefficients from McKenzie and O'Nions [23,24]. Here we report results from both anhydrous melting (pMELTS) runs and wet (pHMELTS) source modeling.

Sources tested include the depleted mantle compositions of McKenzie and O'Nions [23] and Workman and Hart [25] (henceforth MO and WH, respectively). However, neither of these sources is sufficiently high in SiO_2 or low in K_2O and CaO to reproduce Galápagos N-MORB trends (see Fig. 2) with the melting conditions specified above. F and T_0 could not be adjusted sufficiently to match these oxide values in the melt without adversely affecting other major element oxide contents and sacrificing constraints on crustal production. Both the anhydrous and hydrous model GSC sources are lower in K, Ti, Ca and P than MO and WH, and significantly higher in SiO_2 (Table 2). When melted to a maximum melt fraction (F_{max}) ~0.19, the dry source produces a crust 5.9 km thick, which is within the observed range (5.6–6.0 km). Our dry model mantle has an entropy of 264.0 J/K, equivalent to a potential temperature of ~1430 °C. Melting begins at an initial pressure (P_0) of 2.47 GPa. Our wet (60 ppm H_2O) mantle has an entropy of 263.5 J/K and begins melting at P_0 ~3.07 GPa, reaching a slightly lower $F_{max} \sim 0.18$. Subsequent fractional crystallization at a pressure (P_F) of 1.0 kb yields reasonable fits to GSC N-MORB trends (Fig. 2). Fractionating phases include olivine followed by plagioclase, which begins crystallizing at 9.1 wt.% MgO, and clinopyroxene, which joins the assemblage at 8.5 wt.% MgO. These are unusually high Mg-contents for the incoming of plagioclase and clinopyroxene in MORB crystallization sequences, however, the rock assemblages appear to support this. Petrographic observations of the N-MORB suite confirms that plagioclase is a

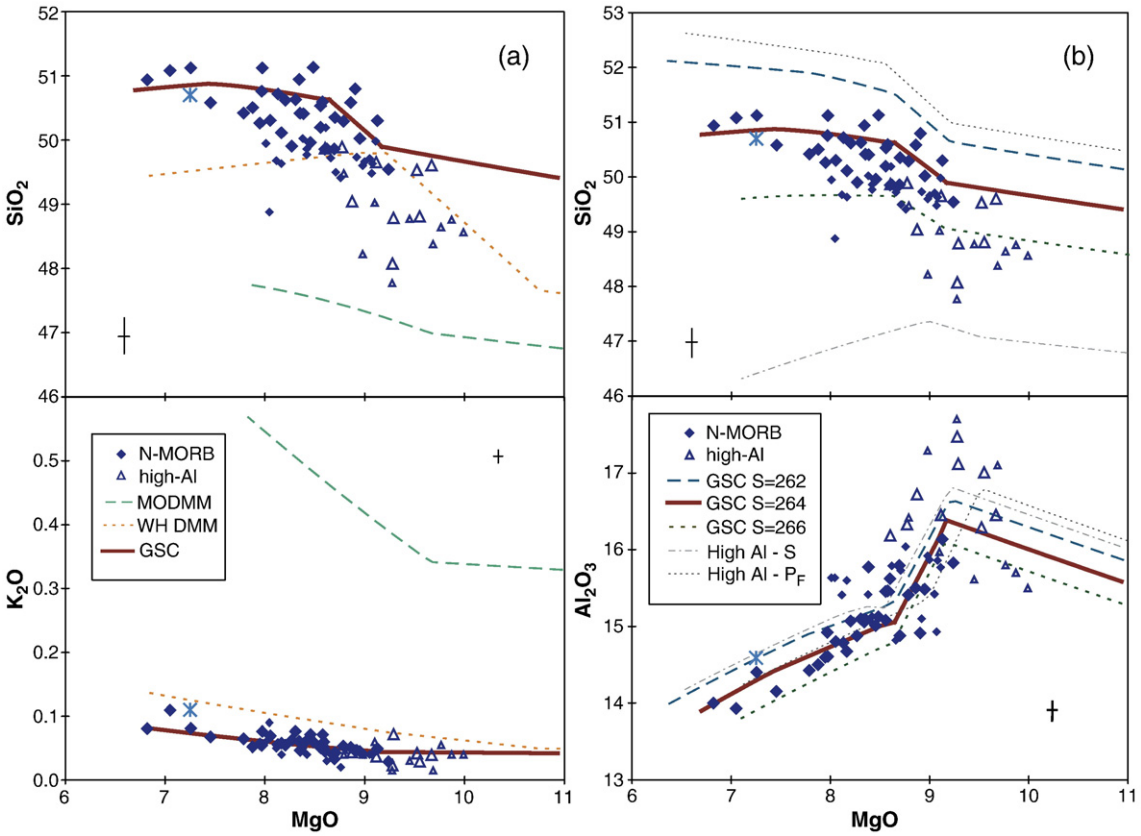

Fig. 2. Galápagos N-MORB (solid symbols) and high-Al (open symbols) sample data — glass (large symbols) and whole-rock XRF (small symbols). (a) Model comparison of 4 sources (MO = McKenzie and O'Nions [23]; WH = Workman and Hart [25]; GSC = modeled N-MORB dry and wet sources — shown as single line due to close overlap), each partially melted to produce a 5.8–5.9-km thick crust. Aggregate melts are fractionated at P_F=1 kb. (b) Effects of entropy on the model (S in units of J/K), based on dry melting runs. S and P_F lines on Al_2O_3 plot represent attempts to reach high Al liquid content with low degrees of partial melting (from low S or high P_F, respectively). Asterisk denotes the average of 118 whole-rock N-MORB analyses from the southern EPR, 13°–23° S (Sinton et al. [40], see text for discussion). High-Al samples chosen using criteria of glass Al_2O_3>16.0 wt.%, MgO>8.5 wt.%, SiO_2<50.0 wt.%. Error bars represent ±1σ standard deviation of glass and whole-rock analyses (larger uncertainty of two analytical techniques shown).

phenocryst phase in virtually all of the high-Mg basalts, and clinopyroxene is present in samples with up to 8.7 wt.% MgO.

Table 2 shows the preferred mantle source compositions determined by pHMELTS modeling (GSC dry and wet sources) compared to other modeled DMMs (global averages from McKenzie and O'Nions [23], Salters and Stracke [26] and Workman and Hart [25]). The pHMELTS-determined sources are extreme mantle compositions — both the wet and dry sources are very high in SiO_2 and extremely depleted in incompatible elements. Our models require a very high CaO/Al_2O_3 ratio in the source to approximate the observed liquid lines of descent. Incompatible elements are lower in the model GSC sources than the McKenzie and O'Nions [23], Workman and Hart [25] and Salters and Stracke [26] global average DMMs. Additionally, the pHMELTS Galápagos source is more depleted than the source modeled by Cushman et al. [3], which uses averages of a more limited selection of oxides to calculate melting extents. The reliability of our modeled source compositions is discussed further in a later section (see Discussion).

5. High-Al MORB

We have identified nine samples from seven locations that contain >16.0 wt.% Al_2O_3 in glass samples with >8.5 wt.% MgO. Corresponding with this enrichment in Al is a slight enrichment in Na, though there appears to be no significant difference in K from normal low-Al MORB (see Figs. 2 and 3). These samples also appear to have slightly higher Fe contents, and are consistently low in Si and Ca. In this paper, we distinguish those samples with glass compositions of >16.0 wt.% Al_2O_3, >8.5 wt.%

Table 2
Modeled GSC source and primary magma compositions, with global average DMMs for comparison

	MO DMM[a]	WH DMM[b]	SS DMM[c]	Cushman et al. GSC[d]	GSC dry source[e]	GSC wet source[e]	GSC primary melt (wet)
SiO_2	45.57	44.71	44.90		47.86	47.86	47.8
TiO_2	0.17	0.13	0.13	0.17	0.10	0.10	0.71
Al_2O_3	2.70	3.98	4.28		2.19	2.20	12.8
Fe_2O_3	0.111	0.191	–		0.07	0.06	0.20
FeO	7.92	8.008	8.07[f]		7.42	7.41	9.14
MgO	40.8	38.73	38.2		40.3	40.3	17.9
CaO	2.41	3.17	3.50		1.90	1.90	9.87
Na_2O	0.24	0.13	0.29	0.23	0.14	0.13	1.48
H_2O	–	–	116	133	–	60	855
K	20	24.9	60	34	10.9	9.8	143
P	40	40.7	40.7		11.3	11.3	134
Cr	3010	3900	2500		300	305	345
Sr	14.7	7.7	9.8		5.4	5	64
V	100	110.0	79		100	100	204
Sc	12	8.6	16.3		8.6	8.6	30

H_2O, K, P, Cr, Sr, V, Sc in ppm, other oxide values in wt.%.
[a] Global average DMM from McKenzie and O'Nions [23].
[b] Global average DMM from Workman and Hart [25].
[c] Global average DMM from Salters and Stracke [26].
[d] GSC oxide concentrations from Cushman et al. [3] hydrous melting model.
[e] Local GSC mantle source, modeled from N-MORB sample compositions assuming a crustal thickness of 5.6–6.0 km. GSC source composition was determined by adjusting the McKenzie–O'Nions DMM to account for the depletion in Ti, Na, K, and P seen in the GSC N-MORB. The modeled continuous melting path for the dry source begins melting at a pressure P_0 of 2.47 GPa with a potential temperature of ~1430 °C, and melts to an F_{max} ~0.19 to produce a crust 5.9 km thick. For the wet source, melting to an F_{max} ~0.18 from P_0 ~3.07 GPa produces a crust 5.8 km thick. Produced melts then crystallize at a crustal pressure of 1.0 kb to produce the GSC N-MORB trends seen in Fig. 2.
[f] Total Fe content (FeO*).

MgO and <50.0 wt.% SiO_2 as high-Al GSC N-MORB. In subsequent sections we evaluate two possible processes to account for these unusual compositions. In our modeling treatment, we assume the high-Al rocks are derived from a similar mantle source as the N-MORB from this area of the ridge. The model runs discussed in the following section use our modeled pHMELTS GSC mantle as the source composition.

5.1. Low-F melting models

Because Al behaves incompatibly during melting, it might be expected that high-Al samples represent low degrees of partial melting. Melting runs with lower entropy values (i.e. cooler mantle) have solidus intersections at shallower depths in the mantle, and proceed to a lower F before accumulating in the crust [27]. However, although lowering F for our GSC mantle source does indeed increase primary magma Al, decreasing F and P_0 also causes an increase in Si (an effect of lower mean pressure of melting as melt Si content is inversely related to pressure of melting [28]), while the high-Al glasses have lower Si values than low-Al MORB at the same MgO (Fig. 2). Alternatively, low F melts can be derived from melting paths with a higher entropy (and correspondingly higher P_0) by extracting melts from deep in the melting region. This process also was modeled, extracting low-F, high-P melts early and then fractionating them at crustal pressures (1–1.5 kb). However, although this process can produce low-Si melts, it fails to produce melts with Al contents as high as required by our data while still matching our other chemical and geophysical constraints (Fig. 2). To increase Al enough to produce the very high values in our rocks under normal crustal fractionation, F has to be decreased so extensively that the modeled crustal production suffers such that the source no longer produces nearly enough melt to form the 5.6–6.0 km of crust seen in this area, and other oxide compositions are overcorrected with model trends lying far outside the observed glass chemistry. Thus, our modeling has not found any satisfactory combination of source composition and melting conditions that yield parental magmas that can account for the observed crustal thickness and reproduce high-Al Galápagos N-MORB compositional trends by low-pressure fractionation. Although simple low-F melting scenarios can produce high-Al melts, these models result in crust that is too thin and magmas

that have significant chemical misfits in other oxides. We conclude from this exercise that we need to consider alternative fractionation paths.

5.2. High-P fractionation models

Although low degrees of partial melting alone cannot explain the high-Al, low-Si chemistry observed in these rocks using this mantle source, we are able to reproduce the compositional variations in our high-Al MORB with models that allow crystallization at pressures up to 0.3–0.4 GPa (Fig. 3). At these pressures, the pyroxene phase volume (stability field) is much larger and clinopyroxene can crystallize very early in the fractionation sequence (up to 10.5 wt.% MgO), driving Al values in the residual melt to higher values while keeping Si values low. Melting for these model runs begins at P_0=2.47 GPa and follows the same temperature adiabat as the dry (pMELTS) N-MORB model. However, because melting is terminated at higher pressures to allow melt aggregation and crystallization in the upper mantle, the maximum extent of melting for high-Al model runs is inherently lower (F_{max} ~ 0.16 for P_F=4 kb) than for the N-MORB melting path (F_{max} ~ 0.19), which allows melting all the way to the base of the lithosphere along the same adiabat. Thus, although low degrees of partial melting alone cannot explain the high-Al chemistry, slightly lower-F melts are built into the high-P crystallization models.

Trace element data on Galápagos high-Al MORB are consistent with evolution involving significant amounts of clinopyroxene crystallization (Fig. 4). The high-Al basalts tend to be low in Cr, Sc, and V, all elements that are partitioned preferentially into clinopyroxene [23,24]. In addition, Sr content is significantly higher than in average N-MORB (Fig. 4). We modeled selected trace elements for the same two-stage melting and fractionation model described above using constant partition coefficients from McKenzie and O'Nions [23,24]. Although the model runs do not match the data trends exactly, probably owing to inapplicability of the chosen partition coefficient values, it is apparent that the effect of early crystallization of clinopyroxene on Cr, Sc, and V concentrations in the high-Al model runs is in the correct direction. In contrast to these elements, Sr shows a clear

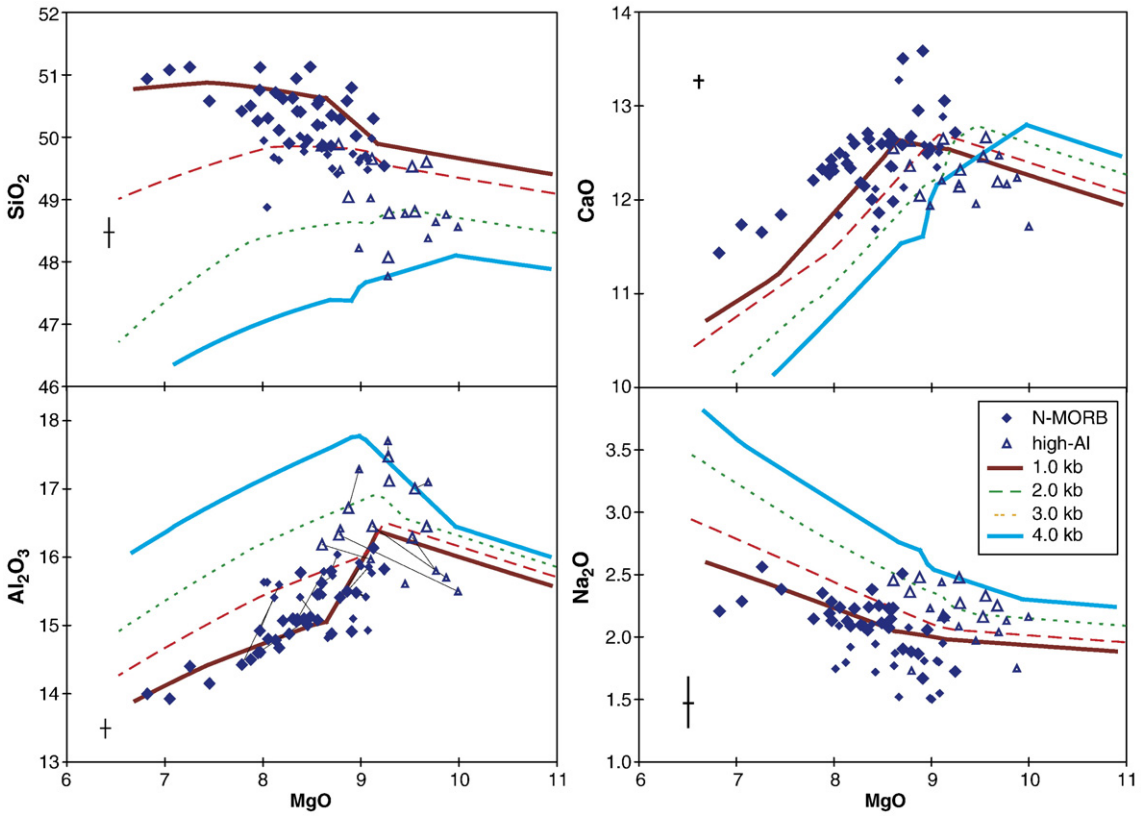

Fig. 3. Modeling of high-Al samples with dry GSC DMM source and variable crystallization processes. Melting starts at 2.47 GPa and proceeds to a pressure P_F, where the melts are aggregated and cooled. Crystallization runs are isobaric and fractional with an oxygen fugacity of FMQ-2. Tie lines in the Al_2O_3 plot denote glass–whole rock pairs.

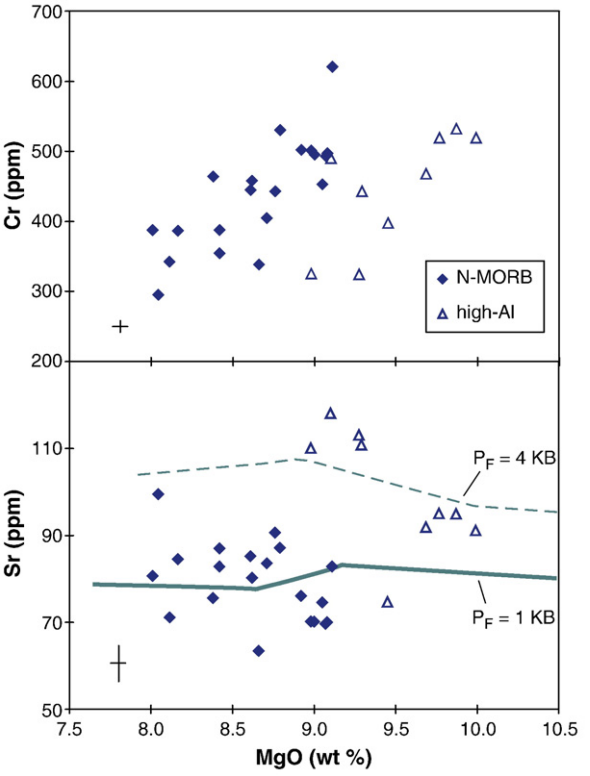

Fig. 4. Sr and Cr trace element data for N-MORB and high-Al samples data — whole-rock XRF analyses. Error bars denote $\pm 1\sigma$ standard deviation of whole-rock analyses (Cr is within symbol size) based on system data reported in Sinton et al. [20]. Sr model runs calculated using constant partition coefficients from McKenzie and O'Nions [23,24] with a source concentration of $Sr_0 = 5.4$ ppm.

separation between the high-Al and normal MORB fractionation paths. High-Al model runs using a crystallization pressure of 4 kb show the ~20 ppm increase in Sr needed to match the high-Al samples, largely an effect of the ~0.03 difference in melt fraction between the two models. The suppression of plagioclase crystallization in the high-Al models help maintain high Sr in the liquid.

The mineralogy produced by these high pressure fractionation runs consists of ~22% olivine (a high value that reflects the high MgO primary melt, an artifact of pMELTS [16]), ~5% plagioclase (An 79), and ~7% clinopyroxene at an MgO of 8.9 wt.%. (see Table 3 for a direct comparison with a specific sample at similar glass MgO). Although the fractionation of clinopyroxene is integral to matching the chemistry of the glasses in these model runs, there are no clinopyroxene phenocrysts observed in our rocks. Plagioclase is typically more abundant in the samples than predicted by fractionation models (by as much as a factor of two in EW 79-1), and often has a higher An content.

6. Discussion

6.1. GSC source

As noted previously, the GSC source composition we derive from (pH)MELTS modeling is extremely depleted in incompatible elements and 2–3 wt.% higher in SiO_2 than WH and MO (Table 2). The high SiO_2 value is required by the (pH)MELTS algorithms to approximate GSC N-MORB SiO_2 content with sufficient melting to create the observed crustal thickness. As P_0 deepens to create sufficient melting, SiO_2 in the resulting melts tends to decrease as a result of the higher pressure, requiring higher values of SiO_2 in the source to compensate and reproduce the observed chemistry. The (pH)MELTS models also require very high CaO/Al_2O_3 in the source (~0.86) to approximate the observed liquid lines of descent for these oxides. This composition requires a large amount of orthopyroxene in the source (>40%) at the expense of olivine and clinopyroxene. Although it might be possible for the mantle in this region to contain local horizons that are anomalously rich in pyroxene, we suspect that the derived GSC source composition could be either an artifact of the (pH)MELTS calculations, or of assumptions about the melting processes that are inherent in these calculations.

The extreme depletion of our modeled GSC source composition is in part an artifact of (pH)MELTS

Table 3
Mineralogy of fractional crystallization model runs compared with sample analysis

	EW 79-1	pMELTS		pHMELTS	
		P_F=1 kb	P_F=3 kb	P_F=1 kb	P_F=3 kb
Liquid					
SiO_2	49.0	50.4	48.6	50.3	48.5
TiO_2	1.01	1.01	1.08	1.02	1.12
Al_2O_3	16.7	15.6	16.8	15.5	16.7
FeO*	9.73	9.20	9.75	9.27	10.0
MgO	8.87	8.85	8.92	8.89	8.85
CaO	12.0	12.6	12.1	12.7	12.1
Na_2O	2.48	2.04	2.38	1.97	2.37
K_2O	0.04	0.05	0.06	0.05	0.06
P_2O_5	0.07	0.08	0.09	0.07	0.09
H_2O	0.16	0.13	0.13	0.12	0.15
Mineral mode					
% ol	1.6	24	22	24	22
Fo	86	83	83	83	83
% plag	15.5	5.4	4.2	5.3	5.1
An	82	80	79	80	79
% cpx	–	–	6.4	–	7

3 kb runs best approximates the glass chemistry of EW 79-1. Model modes represent total fractionated phases.

calculations. Testing of the (pH)MELTS algorithms against MORB experimental data has revealed a number of discrepancies. Calculated liquid MgO is too high [16], which accounts for the high value of our primary magma (17.9 wt.%). Na is known to be too incompatible in MELTS calculations, in which the multiple saturation slope is too steep, causing it to be high in calculated liquid compositions [29]. The high MgO content of the primary magma results in substantial fractionation and a potentially large error in Na, meaning the source must be artificially low to compensate.

In addition, certain assumptions about the melting process may contribute to the extreme values we need for our source. Our model assumes perfect passive flow in which all melts are integrated to produce the crust. Any dynamical effects would decrease the concentration of incompatible elements in the aggregated melts by excluding some of the lowest F melts from the corners of the melt regime. Any amount of active upwelling would decrease the amount of source depletion required to reproduce the low K, Ti, and P values of the sample glasses, and Si in the source would decrease to more reasonable values (a consequence of normalizing with increased incompatibles as well as the effect of needing higher pressures to produce the given amount of melt needed). As a comparison, an end-member active upwelling model using pHMELTS in which all streamlines are the height of the full (1-D) melting column gives us a source with approximately 42 wt.% SiO_2, 2.7 wt.% Al_2O_3 and 0.27 wt.% Na_2O for our crustal thickness. Although pure active upwelling also is unlikely to be realistic for our ridge setting, some component of dynamic flow could help explain our relatively depleted N-MORB samples. As has been noted by Asimow et al. [22], MELTS is unable to produce average MORB crust with the K_2O/TiO_2 ratios seen in depleted MORB (<0.09) with any reasonable amount of K_2O in the source. Considerations of dynamical effects that exclude some of the lower F melts from the aggregate seem to be required in order to successfully model depleted MORB.

There are additional process assumptions inherent in the thermodynamic calculations of MELTS and (pH) MELTS (see Ghiorso and Sack [8], Ghiorso et al. [16] for further explanation of these algorithms). Perhaps most significantly, (pH)MELTS assumes the system is closed during melt migration, such that no mixing or contamination occurs as the melt rises through the mantle. Although there is good evidence that melt migration is not a closed system process (e.g., [30,31]), we have not considered the consequences of reactive flow processes in our modeling. We do not have textural evidence for any disequilibrium processes or mineral assimilation, and we are able to explain the observed chemistry without invoking such processes.

An additional assumption in our model is that melting continues all the way to the base of the crust. Recent studies indicate melting may actually stop at some distance below the Moho [32–34]. Melting accompanies mantle upwelling until the mantle reaches the thermal boundary layer which defines the final melting pressure (P_f). This boundary is primarily controlled by the conductive thermal gradient, which Niu [31] and Niu and Hékinian [35] argue to be spreading rate dependent. Because a precise determination of P_f is currently unconstrained, we chose to model N-MORB melting using the assumption of earlier MORB genesis models that melting continues to the Moho rather than pick an equally arbitrary P_f at some depth below. If melting terminates at a higher P_f, the solidus intersection at P_0 would also need to be deeper to maintain high enough melt fractions to match crustal production and some adjustments of source chemistry would be necessary (higher SiO_2, possibly lower FeO*). Finally, our assumed melt productivity is susceptible to uncertainties in the crustal thickness estimate from multichannel seismic reflection and seafloor refraction data [1,14].

Although our modeled source is unlikely to be a realistic composition for the bulk mantle below this part of the GSC, we are unable to separate the relative contributions from partitioning errors in the MELTS models from the uncertainty in the melting process. Nevertheless, GSC N-MORB are depleted in incompatible elements relative to global average MORB. Since the crustal thickness in this area is close to (or below) average, the qualitative result of the MELTS modeling that we have a depleted source is probably valid. Such depletion could arise from prior melting beneath the East Pacific Rise coupled to an eastwardly flowing asthenosphere [36–38] as previously invoked to explain the abundance of highly depleted lavas from Hole 504B [39] and the relative dearth of T-MORB along the GSC compared to the Southern East Pacific Rise (SEPR) [40].

Given the uncertainties in asthenospheric flow patterns and the lack of comparable studies of crustal thickness and mantle melting along the SEPR, the origin and extent of western GSC major element source depletion remains equivocal. Nevertheless, despite uncertainties in our source composition modeling, the process assumptions and MELTS uncertainties are internally consistent in our comparison between the high-Al, low-Si samples we find near ridge segment terminations, and normal Galápagos MORB.

6.2. High-Al MORB

Clinopyroxene crystallization is integral to creating the high-Al, low-Si signatures seen in the GSC samples. Once melts pass out of the adiabatic upwelling and melting regime and into the region of conductive cooling, they will begin to crystallize minerals on the liquidus. Normally this process occurs at low pressure for mid-ocean ridges where the olivine phase volume (stability field) is large, leading to the olivine± plagioclase crystallization recognized in MORB chemical signatures and excess olivine content in abyssal peridotites sampled at mid-ocean ridges [31]. However, at higher pressures corresponding to depths modeled for GSC high-Al MORB, clinopyroxene precedes plagioclase in joining olivine as a crystallizing phase. Because these mineral phases are largely not seen in the GSC samples (only 1–2% olivine in the rocks vs. the 8% fractionated, and no clinopyroxene phenocrysts present), we suppose that these mineral phases are left behind (possibly as wehrlitic horizons) as the melt continues migrating towards the surface. Upper mantle crystallization involving olivine and clinopyroxene±spinel is well known in the shallow mantle sections of many ophiolites (e.g., [41,42]). Our models predict crystallization beginning as deep as 4 kb, or as much as 6–10 km below the Moho, which is somewhat deeper than currently recognized in the best documented ophiolites [30].

Many models of MORB paragenesis require early, cryptic crystallization of clinopyroxene and this problem has been widely referred to as the "pyroxene paradox", wherein rock chemistry requires clinopyroxene fractionation at some stage in its evolution, but the mineral is absent in the lavas and unstable in the liquids at low pressures (e.g., [43–45]). Among the various explanations for the pyroxene paradox (see Sinton and Detrick [46] for a review) is high-pressure crystallization during or prior to magma ascent and either dissolution or segregation of clinopyroxene during low pressure olivine+plagioclase crystallization (e.g., [45,47,48]).

The GSC high-Al samples are not unique in requiring upper mantle partial crystallization to explain chemical characteristics. Gabbros, megacrysts and cumulate phases believed to be derived from upper mantle fractionation have been found at slow spreading ridges and fracture zones [49–51]. Other petrological evidence from MORB geochemistry suggests that partial crystallization occurs in the mantle as well as the crust [13,45,48,52–54,60,61].

Our model shows that Galápagos high-Al MORB can be derived from the same mantle source as the GSC N-MORB without requiring source heterogeneity. Because Galápagos high-Al MORB do not exhibit any K or Ti enrichment, an added component enriched only in Al seems unlikely. As mentioned previously, there are additional processes that can increase glass Al content that must be considered. Wet melting experiments have yielded plagioclase-rich, high-Al basalts [55], and water is known to play a role in the formation of high-Al calc-alkaline rocks [9]. However, the low water content in GSC N-MORB [3] makes this an unlikely alternative, and GSC high-Al samples that have been analyzed for water have the same low H_2O contents (0.14–0.16 wt.%) as normal low-Al N-MORB at the same MgO. Plagioclase assimilation is an alternative process that can increase the aluminum content in magmas [56,57]. However, we see no textural evidence for mineral assimilation, and the high-Al signature appears in both glass and whole-rock data, with the exception of two sites: the nearly aphyric EW-71 (samples a and b) and ALV-1554, for which whole-rock data have low Al, despite corresponding low Si and Ca, and higher Na (other signatures of early fractionation). A comparison of the glass and whole-rock data for these samples indicates they may not have undergone any significant plagioclase or clinopyroxene fractionation—glass–rock tie-lines appear to outline an olivine-only fractionation vector (Fig. 3). Thus, although these samples exhibit at least some of the characteristics of the more extreme high-Al N-MORB, high pressure evolution is not required. Along the GSC those samples that appear to require significant high pressure fractionation may be restricted to those with >16.5 wt.% Al_2O_3.

It is important to note that our fractional crystallization runs are isobaric and assume melt congregates and fractionates at a single depth. In fact, crystallization may be polybaric, proceeding en route while the melt is migrating upwards to the crust, or multi-stage, with high-pressure fractionation followed by low-pressure crustal fractionation. While the high-pressure crystallization may occur in upper mantle magma chambers, this is certainly not required by the data. Polybaric or multi-stage fractionation modeling would require initial crystallization at higher pressures than our isobaric model to achieve the same glass composition: by crystallizing first at higher pressures (ol+cpx), liquids can achieve higher Al_2O_3 contents at higher MgO, then crystallize at low pressure (ol+plag), decreasing both Al_2O_3 and MgO to reach their target melt composition. Because crystallization begins at higher MgO contents for these models, more crystallization occurs overall, perhaps explaining why we find larger amounts of plagioclase in some of these samples than the isobaric model mode predicts (Table 3). Because adding a low-pressure crystallization

stage into the model requires that we initiate crystallization at higher pressure, our isobaric pressure estimates for the onset of crystallization are likely minimum values. Glass–whole-rock tie-lines of the highest Al samples seem to support this, delineating fractionation vectors from even higher Al_2O_3 values than our 4 kb model runs are able to obtain (Fig. 3).

6.3. Global distribution

The global distribution of MORB with >16.0 wt.% Al_2O_3 and >8.5 wt.% MgO (Fig. 1) indicates that they occur preferentially at ridges with slow to intermediate spreading rates and at the ends of ridge segments. Along the western GSC, these samples are restricted to the ends of (possibly dying) ridge segments near the 95.5° W propagator (see Fig. 1). We have not found high-Al and N-MORB occurring within single dredge sites.

Slow-spreading ridges and ridge segment terminations are areas where steady-state magma chambers are unlikely to be present [46]. Conductive cooling to the surface also has a greater effect on the mantle temperature profile in these regions than at fast-spreading ridges due to slower upwelling. Consequently, melting might stop at significantly deeper levels beneath slow-spreading ridges and fracture zones than at fast-spreading ridges, where the conductive thermal gradient has less of an effect against the adiabat (convective gradient) [35,58,59]. High-pressure fractionation is enhanced by conductive cooling in these regions, causing clinopyroxene and olivine to fractionate in the upper mantle. This is consistent with the findings of Michael and Cornell [60], who found partial crystallization pressures were correlated with spreading rate, and Dmitriev [54], who associated high pressures of partial crystallization with ridge terminations (including fracture zones, overlapping spreading centers, and devals). Herzberg [61] modeled partial crystallization in the mantle based on An–Di–En projections and found the same correlation between ridge setting and high pressure MORB crystallization. Application of his petrological model to GSC MORB data gives crystallization pressures ranging from 0.48–0.85 GPa for the high-Al samples, compared with an average of 0.14 GPa for normal low-Al GSC N-MORB (written comm., 2005) — a factor of 2 greater than the pressures estimated by our isobaric fractionation modeling but probably within the range of errors associated with the two approaches. As noted in the previous section, our crystallization pressures are likely minima, and non-isobaric crystallization may require deeper solidus intersections to achieve the high-Al, low-Si signature characteristic of fractionation in the upper mantle.

7. Summary

Forward modeling of Galápagos Spreading Center N-MORB using (pH)MELTS requires a highly depleted peridotite mantle source with a maximum melt fraction of ~0.19 and a potential temperature of ~1430 °C. When aggregated and cooled in the shallow crust (1 kb), these melts follow fractional crystallization paths that approximate our N-MORB glass compositions. The rather extreme mantle source required by this model is partly a result of errors in the MELTS thermodynamic calculations exacerbated by the process assumptions of perfect passive flow and complete melt focusing. The results of this exercise illustrate some of the limitations of quantitative thermodynamic modeling without a corresponding flow model.

Several high-Mg GSC glass samples contain unusually high concentrations of Al, along with low Si and abundant plagioclase phenocrysts. Although high-Al contents can be obtained by very low extents of partial melting, low-F models result in significant misfits in other major element oxides and do not explain the sample chemistry. Instead, we require high-pressure fractional crystallization of clinopyroxene at pressures of 0.3–0.4 GPa to explain major element compositions of these samples. Although clinopyroxene is not present as a phenocryst phase in these samples, trace element data are qualitatively consistent with clinopyroxene fractionation. Crystallization in the upper mantle is consistent with other recent models correlating high-pressure crystallization with slow spreading ridges and ridge segment terminations. High-pressure crystallization is enhanced by conductive cooling in these regions, causing olivine and clinopyroxene to fractionate in the upper mantle.

Acknowledgments

We thank the shipboard scientific party and crew of R/V *Maurice Ewing* Leg EW00-04 for their help in the data and sample acquisition, and the Ecuadorian government and the Parque Nacional Galápagos for permission to work in their waters. We also thank John Mahoney and David Graham for their expert dredging, Kent Ross for his assistance with the microprobe and XRF analyses, Buffy Cushman for glass data collection, Chuck Fraley for his help with the whole-rock analyses, and JoAnn Sinton for thin section preparation. Discussions with

Julia Hammer, Kevin Johnson and Rhea Workman have helped clarify many of the ideas in this paper. We greatly appreciate the careful, detailed reviews by Emily Klein and Paul Asimow. This research was supported by the National Science Foundation grants OCE03-27051 and OCE05-24922. This is SOEST contribution #6978.

Appendix A. Supplementary data

Supplementary data associated with this article can be found, in the online version, at doi:10.1016/j.epsl.2006.09.048.

References

[1] R. Detrick, J. Sinton, G. Ito, J. Canales, M. Behn, T. Blacic, B. Cushman, J. Dixon, D. Graham, J. Mahoney, Correlated geophysical, geochemical and volcanological manifestations of plume–ridge interaction along the Galápagos spreading center, Geophys. Geochem. Geosyst. 3 (2002), doi:10.1029/2002GC000350.

[2] C. DeMets, R. Gordon, D. Argus, S. Stein, Effect of recent revisions to the geomagnetic time reversal scale on estimates of current plate motions, Geophys. Res. Lett. 21 (1994) 2191–2194.

[3] B. Cushman, J. Sinton, G. Ito, J. Dixon, Glass compositions, plume–ridge interaction, and hydrous melting along the Galápagos Spreading Center, 90.5°W to 98°W, Geochem. Geophys. Geosyst. 5 (2004), doi:10.1029/2004GC000709.

[4] J.-G. Schilling, R. Kingsley, J. Devine, Galápagos hot-spot spreading center system I. Spatial petrological and geochemical variations (83°W–101°W), J. Geophys. Res. 87 (1982) 5593–5610.

[5] M. Fisk, A. Bence, J.-G. Schilling, Major element chemistry of Galápagos rift zone magmas and their phenocrysts, Earth Planet. Sci. Lett. 61 (1982) 171–189.

[6] S. Verma, J.-G. Schilling, Galápagos hot spot-spreading center system 2. $^{87}Sr/^{86}Sr$ and large ion lithophile element variations (85°W–101°W), J. Geophys. Res. 87 (1982) 10838–10856.

[7] S. Verma, J.-G. Schilling, D. Waggoner, Neodymium isotopic evidence for Galápagos hotspot-spreading centre system evolution, Nature 306 (1983) 654–657.

[8] M. Ghiorso, R. Sack, Chemical mass-transfer in magmatic processes IV. A revised and internally consistent thermodynamic model for the interpolation and extrapolation of liquid–solid equilibria in magmatic systems at elevated-temperatures and pressures, Contrib. Mineral. Petrol. 199 (1995) 197–212.

[9] T. Sisson, T. Grove, Experimental investigation of the role of H_2O in calc-alkaline differentiation and subduction zone magmatism, Contrib. Mineral. Petrol. 113 (1993) 143–166.

[10] Y. Panjasawatwong, L. Danyushevsky, A. Crawford, K. Harris, An experimental study of the effects of melt composition on plagioclase-melt equilibria at 5 and 10 kbar: implications for the origin of magmatic high-An plagioclase, Contrib. Mineral. Petrol. 118 (1995) 420–432.

[11] A. Sobolev, L. Danyushevsky, L. Dmitriev, N. Suschevskaya, High-alumina magnesian tholeiite as the primary basalt magma at midocean ridge, Geochem. Int. 26 (1989) 128–133.

[12] R. Nielsen, J. Crum, R. Bourgeois, K. Hascall, L. Fisk, D. Christie, Melt inclusions in high-An plagioclase from the Gorda Ridge: an example of the local diversity of MORB parent magmas, Contrib. Mineral. Petrol. 122 (1995) 34–50.

[13] W. Meurer, M. Sturm, E. Klein, J. Karson, Basalt compositions from the Mid-Atlantic Ridge at the SMARK area (22°30′N to 22°50′N): implications for parental liquid variability at isotopically homogeneous spreading centers, Earth Planet. Sci. Lett. 186 (2001) 451–469.

[14] J. Canales, G. Ito, R. Detrick, J. Sinton, Crustal thickness along the Galápagos Spreading Center and the compensation of the Galápagos hotspot swell, Earth Planet. Sci. Lett. 203 (2002) 311–327.

[15] P. Asimow, M. Ghiorso, Algorithmic modifications extending MELTS to calculate subsolidus phase relations, Am. Mineral. 83 (1998) 1127–1132.

[16] M. Ghiorso, M. Hirschmann, P. Reiners, V. Kress, The pMELTS: a revision of MELTS for improved calculation of phase relations and major element partitioning related to partial melting of the mantle to 3 GPa, Geochem. Geophys. Geosyst. 3 (2002), doi:10.1029/2001GC000217.

[17] P. Smith, P. Asimow, Adiabat_1ph: a new public front-end to the MELTS, pMELTS, and pHMELTS models, Geochem. Geophys. Geosyst. 6 (2005), doi:10.1029/2004GC000816.

[18] K. Norrish, J. Hutton, An accurate X-ray spectrographic method for the analysis of a wide range of geological samples, Geochim. Cosmochem. Acta 33 (1977) 431–441.

[19] B. Chappell, Trace element analysis of rocks by X-ray spectrometry, Adv. X-ray Anal. 34 (1992) 263–276.

[20] J. Sinton, K. Groenvold, K. Saemundsson, Eruptive history of the Western Volcanic Zone, Iceland, Geochem. Geophys. Geosyst. 6 (2005), doi:10.1029/2005GC0010121.

[21] P. Asimow, J. Dixon, C. Langmuir, A hydrous melting and fractionation model for mid-ocean ridge basalts: application to the Mid-Atlantic Ridge near the Azores, Geochem. Geophys. Geosyst. 5 (2004), doi:10.1029/2003GC000568.

[22] P. Asimow, M. Hirschmann, E. Stolper, Calculation of peridotite partial melting from thermodynamic models of minerals and melts, IV. Adiabatic decompression and the composition and mean properties of mid-ocean ridge basalts, J. Petrol. 42 (2001) 963–998.

[23] D. McKenzie, R. O'Nions, Partial melt distributions from inversion of rare-earth element concentrations, J. Petrol. 32 (1991) 1021–1091.

[24] D. McKenzie, R. O'Nions, The source regions of ocean island basalts, J. Petrol. 36 (1995) 133–159.

[25] R. Workman, S. Hart, Major and trace element composition of the depleted MORB mantle (DMM), Earth Planet. Sci. Lett. 231 (2005) 53–72.

[26] V. Salters, A. Stracke, Composition of the depleted mantle, Geochem. Geophys. Geosyst. 5 (2004), doi:10.1029/2003GC000597.

[27] E. Klein, C. Langmuir, Global correlations of ocean ridge basalt chemistry with axial depth and crustal thickness, J. Geophys. Res. 92 (1987) 8089–8115.

[28] A. Jaques, D. Green, Determination of liquid compositions in high-pressure melting of peridotite, Am. Mineral. 64 (1979) 1312–1321.

[29] M. Hirschmann, M. Ghiorso, L. Wasylenki, P. Asimow, E. Stolper, Calculation of peridotite partial melting from thermodynamic models of minerals and melts. I. Review of methods and comparison to experiments, J. Petrol. 39 (1998) 1091–1115.

[30] P. Kelemen, G. Hirth, N. Shimizu, M. Spiegelman, H. Dick, A review of melt migration processes in the adiabatically

upwelling mantle beneath oceanic spreading ridges, Philos. Trans. R. Soc. Lond. 355 (1997) 283–318.
[31] Y. Niu, Mantle melting and melt extraction processes beneath ocean ridges: evidence from abyssal peridotites, J. Petrol. 38 (1997) 1047–1074.
[32] Y. Niu, R. Batiza, An empirical method for calculating melt compositions produced beneath mid-ocean ridges: application for axis and off-axis (seamounts) melting, J. Geophys. Res. 96 (1991) 21753–21777.
[33] Y. Shen, D. Forsyth, Geochemical constraints on initial and final depth of melting beneath mid-ocean ridges, J. Geophys. Res. 100 (1995) 2211–2237.
[34] R. White, T. Minshull, M. Bickle, C. Robinson, Melt generation at very slow-spreading oceanic ridges: constraints from geochemical and geophysical data, J. Petrol. 42 (2001) 1171–1196.
[35] Y. Niu, R. Hékinian, Spreading rate dependence of the extent of mantle melting beneath ocean ridges, Nature 385 (1997) 326–329.
[36] R. Bostrom, Westward displacement of the lithosphere, Nature 234 (1971) 356–538.
[37] R. Ricard, C. Doglioni, R. Sabadini, Differential rotation between lithosphere and mantle: a consequence of lateral viscosity variations, J. Geophys. Res. 96 (1991) 8407–8415.
[38] C. Doglioni, E. Carminati, E. Bonatti, Rift asymmetry and continental uplift, Tectonics 22 (2003), doi:10.1029/2002TC001459.
[39] L. Autio, J. Rhodes, Costa Rica Rift Zone basalts: geochemical and experimental data from a possible example of multistage melting, Initial Rep. DSDP 69 (1983) 729–745.
[40] J. Sinton, S. Smaglik, J. Mahoney, K. Macdonald, Magmatic processes at superfast spreading mid-ocean ridges: glass compositional variations along the East Pacific Rise, 13°–23°, J. Geophys. Res. 96 (1991) 6133–6155.
[41] J. Sinton, Equilibration history of the basal Alpine-type peridotite, Red Mountain, New Zealand, Ofioliti 3 (1978) 224.
[42] P. Kelemen, N. Shimizu, V. Salters, Extraction of mid-ocean-ridge basalt from the upwelling mantle by focused flow of melt in dunite channels, Nature 375 (1995) 747–753.
[43] M. Dungan, J. Rhodes, Residual glasses and melt inclusions in basalts from DSDP Legs 45 and 46: evidence for magma mixing, Contrib. Mineral. Petrol. 67 (1978) 417–431.
[44] D. Francis, The pyroxene paradox in MORB glasses — a signature of picritic parental magmas? Nature 319 (1980) 586–588.
[45] D. Elthon, D. Ross, J. Meen, Compositional variations of basaltic glasses from the Mid-Cayman Rise spreading center, J. Geophys. Res. 100 (1995) 12497–12512.
[46] J. Sinton, R. Detrick, Mid-ocean ridge magma chambers, J. Geophys. Res. 97 (1992) 197–216.
[47] G. Thompson, W. Bryan, W. Melson, Geological and geophysical investigations of the mid-Cayman rise spreading center: geochemical variation and petrogenesis of basalt glasses, J. Geol. 88 (1980) 41–55.
[48] T. Grove, R. Kinzler, W. Bryan, Fractionation of mid-ocean ridge basalts, in: J. Phipps-Morgan, D. Blackman, J. Sinton (Eds.), Mantle Flow and Melt Generation at Mid-Ocean Ridges, Geophys. Monogr. Ser., vol. 71, AGU, Washington, DC, 1992, pp. 281–310.
[49] D. Elthon, J. Casey, S. Komor, Mantle chemistry of ultramafic cumulates from the North Arm Mountain Massif of the Bay of Islands ophiolite: evidence for high-pressure crystal fractionation of oceanic basalts, J. Geophys. Res. 87 (1982) 8717–8734.
[50] D. Stakes, J. Shervais, C. Hopson, The volcanic–tectonic cycle of the FAMOUS and AMAR valleys, Mid-Atlantic Ridge (36°47′N): evidence from basalt glass and phenocryst compositional variations for a steady state magma chamber beneath valley midsections, AMAR 3, J. Geophys. Res. 89 (1984) 6995–7028.
[51] D. Elthon, Petrology of gabbroic rocks from the mid-Cayman rise spreading center, J. Geophys. Res. 92 (1987) 658–682.
[52] D. Tormey, T. Grove, W. Bryan, Experimental petrology of normal MORB near the Kane Fracture Zone: 22°–25°N, Mid-Atlantic Ridge, Contrib. Mineral. Petrol. 96 (1987) 121–139.
[53] R. Kinzler, T. Grove, Primary magmas of mid-ocean ridge basalts, 2. Applications, J. Geophys. Res. 97 (1992) 6907–6926.
[54] L. Dmitriev, Chemical variability of mid-ocean ridge basalts as a function of the geodynamic setting of their formation, Petrology 6 (1998) 314–334.
[55] J. Beard, G. Lofgren, An experiment-based model for the petrogenesis of high-alumina basalts, Science 258 (1992) 112–115.
[56] M. Flower, Accumulation of calcic plagioclase in ocean ridge tholeiite: an indication of spreading rate? Nature 287 (1980) 530–532.
[57] L. Danyushevsky, M. Perfit, S. Eggins, T. Falloon, Crustal origin for coupled 'ultra-depleted' and 'plagioclase' signatures in MORB olivine-hosted melt inclusions: evidence from the Siqueiros Transform Fault, East Pacific Rise, Contrib. Mineral. Petrol. 144 (2003) 619–637.
[58] Y. Bottinga, C. Allègre, Partial melting under spreading ridges, Philos. Trans. R. Soc. Lond. 288 (1978) 501–525.
[59] I. Reid, H. Jackson, Oceanic spreading rate and crustal thickness, Mar. Geophys. Res. 5 (1981) 165–172.
[60] P. Michael, W. Cornell, Influence of spreading rate and magma supply on crystallization and assimilation beneath mid-ocean ridges: evidence from chlorine and major element chemistry of mid-ocean ridge basalts, J. Geophys. Res. 103 (1998) 18325–18356.
[61] C. Herzberg, Partial crystallization of mid-ocean ridge basalts in the crust and mantle, J. Petrol. 45 (2004) 2389–2405.
[62] R. Hey, J. Sinton, M. Kleinrock, R. Yonover, K. Macdonald, S. Miller, R. Searle, D. Christie, T. Atwater, N. Sleep, H. Johnson, C. Neal, ALVIN Investigation of an active propagating rift system, Galápagos 95.5°W, Mar. Geophys. Res. 14 (1992) 207–226.
[63] J. Sinton, R. Detrick, J. Canales, G. Ito, M. Behn, Morphology and segmentation of the western Galápagos Spreading Center, 90.5°–98°W: plume–ridge interaction at an intermediate spreading ridge, Geochem. Geophys. Geosyst. 4 (2003), doi:10.1029/2003GC000609.
[64] K. Lehnert, Y. Su, C. Langmuir, B. Sarbas, U. Nohl, A global geochemical database structure for rocks, Geochem. Geophys. Geosyst. 1 (2000), doi:10.1029/1999GC000026.